ACS APPLIED MATERIALS & INTERFACES

www.acsami.org

Research Article

Flying Squirrel-Inspired Motion Control of a Light-Deformed Pt-PAzoMA Micromotor through Drag Force Manipulation

Xinyi Lin, Borui Xu, Zhe Zhao, Xiaoyan Yang, Yi Xing, Chunyu You, Ye Kong, Jizhai Cui, Liangliang Zhu, Shaoliang Lin,* and Yongfeng Mei*

Cite This: *ACS Appl. Mater. Interfaces* 2021, 13, 30106–30117

Read Online

ACCESS | Metrics & More | Article Recommendations | Supporting Information

ABSTRACT: Micromotors require stable and precise motion control for complex tasks such as microsurgery, drug delivery *in vivo*, or environmental monitoring *ex vivo*. However, a continuous control signal is needed for micromotors to achieve motion control during their whole journey, which hinders their application in areas where external control stimuli are limited or unavailable. Fortunately, nature suggests an excellent solution that flying squirrel exhibits motion tuning capability by deforming itself when jumping off a tall tree. Inspired by this, we propose a Pt-PAzoMA Janus micromotor that precisely changes its shape (from a spherical shape to an elliptical shape) under a brief light signal (450 nm) and maintains this deformation until next signal reception. The deformed elliptical micromotor performs relatively low-speed motion compared to the spherical one, which is further confirmed by massive simulation results. In addition, by investigating motion behavior experimentally and theoretically, it is proved that the motion modulation is caused by the drag force changing brought from the deformation. This method represents a different route to regulate the motion of micromotors without a continuous signal, which is useful in application scenarios where the environmental control signal is inaccessible/limited or long-time operation with minimum energy input is required to maintain motion manipulation. With further function modification, this kind of shape-changing micromotor has potential in optimizing drug diffusion efficiency by speed altering and long-term monitoring at the diseased area by confining the active range of the micromotor in the targeted area through deformation.

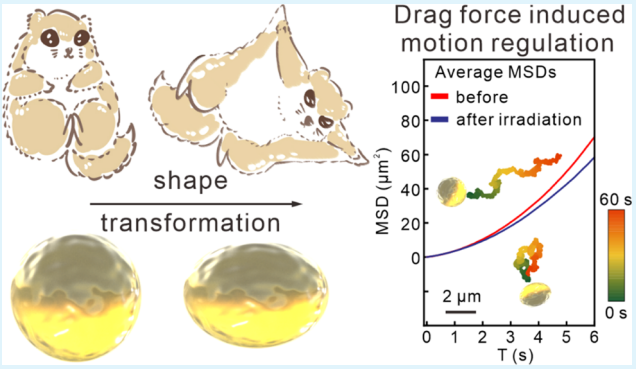

KEYWORDS: *micromotor, motion control, drag force manipulation, photo-deformation, PAzoMA*

1. INTRODUCTION

Micromotors are a family of microsize devices that propel themselves autonomously by transferring chemical or physical energy into mechanical energy.[1] The long distance of dynamic motion, together with their tiny size and easily modified surface,[2,3] promises the future of micromotors toward a blaze of applications from microsurgery[4] and drug delivery[5−7] to sensing[8,9] and pollutant removal.[10,11] To achieve these complex tasks, especially *in vivo* operations, it is essential to control the micromotors' motion precisely and stably. What is more, motion control is the basis of swarm-behaved robotics and their interaction, either for self-organization or for coherent motion.[12,13] By now, a lot of motion regulation methods have been explored, most of which are dependent on changing propulsive force.[14] The motion of catalytic micromotors can be modulated by the concentration of fuels or the reaction temperature.[15] Applying magnetic field can alter the speed and direction of micromotors consisting of magnetic segments.[16,17] Other physical signals such as light,[18−22] ultrasound,[23] electric,[24] and temperature field[25] are also used to regulate the motion of micromotors by generating corresponding field gradients. These motion control methods rely exclusively on the continuous reception of motion control signals.[12,26,27] As a result, motion disruption may occur and the micromotor may deviate from its designed route when the signal reception is not stable due to environmental disruption or short signal transmission range. For example, magnetic-controlled deformable micromotors could alter their shapes repeatedly under magnetic field for controllable self-propulsion.[28,29] Without consistent reception of the motion control signal, the deformed shape could not preserve and thus the motion regulation fails. From this perspective, a stable motion

Received: April 25, 2021
Accepted: June 9, 2021
Published: June 18, 2021

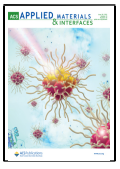

https://doi.org/10.1021/acsami.1c07569
ACS Appl. Mater. Interfaces 2021, 13, 30106−30117

modulation method without the requirement of continuous control signal is required.

In natural world, flying squirrel, pushing itself off a large branch of a tree, stretches out its limbs so that two folds of skin along the body fan out like sails, increasing air drag for safe landing. This motion regulation avoids continuous control signals simply by changing shapes under a short brain signal and keeping the altered posture in the following movements. The motion behavior indicates that a sustaining alter in motion can be obtained if the targeted object deforms after proper stimuli and keeps the transformation, rather than continuously receiving modulation from the external control signal. Herein, we present a flying squirrel-inspired strategy to regulate motion in microworld, where the shape of a spheroidal Janus micromotor is altered and the altered shape is maintained until next signal reception. The Janus micromotor consists of a homopolymer poly[6-(4-methoxy-4′-oxyazobenzene)hexyl methacrylate] (PAzoMA) particle with Pt half-coating on the surface. Upon 450 nm blue linear polarized light (LPL) irradiation, the Pt-PAzoMA Janus micromotor deformed into an ellipsoid with a desired aspect ratio. The slowdown in the motion of the micromotors after deformation is fully uncovered using mean square displacements (MSDs) and speed. The simulated MSD and speed curves are highly accorded with the experimental results. In addition, by theoretical calculation, we prove that the motion regulation is caused by the change of drag force.

We further extend the versatile motion manipulation concept to other micromotors in the Discussion section. The control strategy is very attractive for applications that need long-time stable motion regulation with minimum energy/signal input or should avoid the side effect of long-time light/magnetic/ultrasound/other control signals to human/animal body. Micromotors with drag force manipulating ability have the potential to be applied for long-term *in vivo* treatment. For example, drag-force-controlled micromotors can get targeted area quickly within a short time and switch the speed to a relatively low level for long-term drug release or microsurgery around the affected area with minimum energy input.

2. EXPERIMENTAL SECTION

2.1. Materials. Atom transfer radical polymerization method was adopted to synthesize PAzoMA homopolymers with azobenzene on the side chain. The molecular weight (M_n) of PAzoMA is 1.3×10^4, and the polydispersity index M_w/M_n is 1.4, as reported before.[30] Hydrogen peroxide (H_2O_2, 30 wt %) was obtained from Hushi Inc., and chloroform was purchased from Sinopharm Chemical Reagent Co., Ltd.

2.2. Fabrication of the Pt-PAzoMA Janus Micromotor with Different Aspect Ratios. A 250 mL wide-mouth glass bottle was taken and 50 mL of ethanol was added into the bottle. A sponge scouring pad was put inside the bottle. Then, the bottle was sealed and put into an incubator with a stable temperature of 40 °C, creating a saturated ethanol vapor atmosphere in the bottle. The PAzoMA homopolymer powder was dissolved first in chloroform-*d* with a concentration of 5 mg mL^{-1} and then added onto a cleaned small glass slide (0.5−1 cm^2). The glass slide was transferred into the glass bottle as soon as possible. After the ethanol and PAzoMA polymer solution were evaporated, microsphere arrays were formed. The small glass slides carrying the microsphere array were then put into an e-beam evaporation chamber to cap microspheres with a 3 nm-thick Pt layer at an evaporation rate of 0.1 Å/s, during which the cavity temperature was around 27 °C. To release microspheres from the substrate, the glass side was tied onto the bottom of a 5 mL beaker and immersed in 1−3 mL of deionized (DI) water. Sonification was applied for 30 min, and the water temperature was controlled at room temperature to release PAzoMA micromotors from the slide. The Pt-PAzoMA micromotor suspension was thus obtained and stored for the following experiments.

For Pt-PAzoMA Janus micromotors with other aspect ratios, one more step for deformation was needed just before the electron beam evaporation (EBE) process. Here, blue light (450 nm) from a LED point light source (COINU UVLED) went through a matched polaroid and becomes LPL, shining on the samples with light illumination (613 ± 3) mW cm^{-2}. After irradiation with different times, ellipsoids with different aspect ratios were obtained, followed by EBE and ultrasound-assisted release.

2.3. Polymer Characterization. Differential scanning calorimetry (DSC) data of the PAzoMA polymer were recorded using a differential scanning calorimeter (TA Instrument, Q2000). Proton nuclear magnetic resonance (^{1}H NMR) of the PAzoMA homopolymer dissolved in deuterated chloroform ($CDCl_3$) solution was measured by a Fourier transform nuclear magnetic resonance spectrometer (400 MHz, AVANCE III HD) with ^{1}H sensitivity ≥ 480:1 (0.1% EB). UV−vis absorption spectra of the PAzoMA homopolymer solution ($CDCl_3$ as a solvent) were obtained on a UV−vis recording spectrophotometer (SHIMADZU UV 2500).

2.4. Morphology Characterization. The optical images of micromotors were captured by an optical microscope (OLYMPUS BX51) connected with a CCD camera. Scanning electron microscopy (SEM) images were taken by a field emission scanning electron microscope (Zeiss Sigma SEM) at 5 kV accelerating voltage to obtain surface morphologies of PAzoMA microspheres and Pt-PAzoMA micromotors both before and after 450 nm LPL irradiation. Before SEM, PAzoMA microspheres were coated with 3 nm Au by EBE at an evaporation rate of 0.1 Å/s for better conductivity. The elemental composition distribution images were mapped using an energy-dispersive spectrometer equipped on the scanning electron microscope.

To collect the statistical data of micromotor geometries, the SEM images of the Pt-PAzoMA micromotors before and after LPL irradiation are imported into FIJI for frontal projected areas and diameters counting using measurement plugin. More than 1700 micromotors are counted for their frontal projected areas both before and after LPL irradiation.

2.5. Motion Recording. A video camera is equipped on a stereoscopic microscope (ST6024-B1 Ruihong) to capture the motion behavior of PAzoMA microspheres, PAzoMA microellipsoid, and Pt-PAzoMA micromotor before and after LPL illumination. The recording rate is 10 frames per second. To observe the motion, 30 μL of PAzoMA microsphere suspension or Pt-PAzoMA micromotor suspension was dribbled onto a cleaned slide, followed by the addition of DI water or H_2O_2 solution under various H_2O_2 concentrations. To obtain tracking statistics, 20 nominally identical Pt-PAzoMA micromotors before and after LPL irradiation were tracked under each H_2O_2 concentration and each micromotor was tracked for at least 60 s.

2.6. Video Analysis. To analyze the videos, the image processing software with plugins package FIJI[31] (http://fiji/sc/) was adopted here. The videos were loaded as image sequences into FIJI, and then plugin Trackmate[32] was used for micromotor tracking to get trajectories of PAzoMA microspheres or Pt-PAzoMA micromotors both before and after LPL illumination. According to the MATLAB per-value class-msdanalyzer (https://tinevez.github.io/msdanalyzer/), a customized MATLAB script was adapted to calculate the MSD of the micromotors in different H_2O_2 concentrations.[20,33]

2.7. Motion Simulation. The trajectories of Pt-PAzoMA Janus micromotors characterized by self-propulsive speed V were simulated by the Langevin equations in a two-dimensional regime.[34] A simulated trajectory program in MATLAB was adopted and adapted to obtain simulated trajectories of spherical and elliptical micromotors.[34] The simulated MSDs were obtained by introducing simulated trajectory data into the MATLAB customized script for MSD calculations. The diffusion coefficients D_T and D_R, as parameters in the equations, could

https://doi.org/10.1021/acsami.1c07569
ACS Appl. Mater. Interfaces 2021, 13, 30106−30117

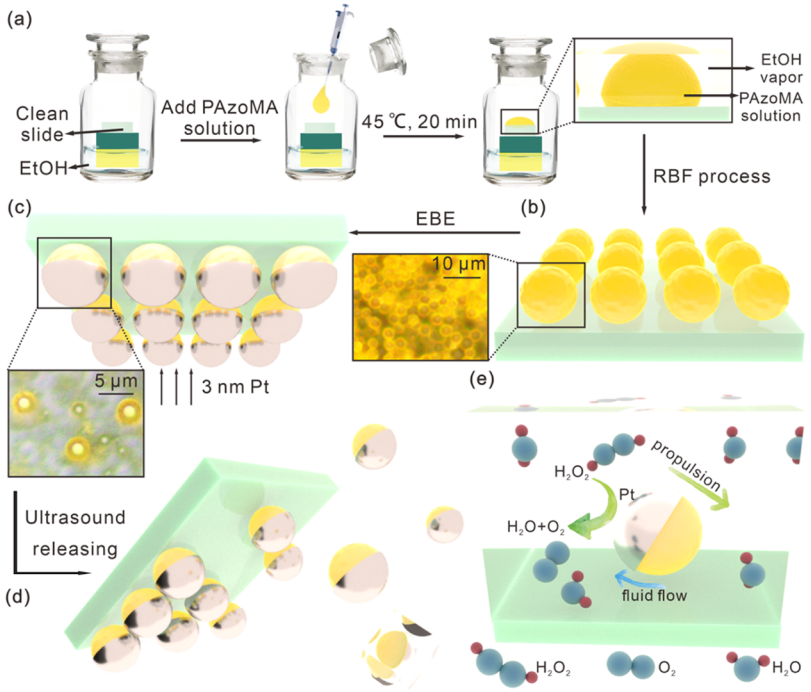

Figure 1. Schematic of fabrication and propulsion of the Pt-PAzoMA micromotor. (a) RBF method for fabricating PAzoMA microspheres; (b) PAzoMA microsphere arrays; (c) capping Pt catalyst by EBE to form Janus structure of the micromotors, and (d) ultrasound releasing of Pt-PAzoMA micromotors from the slide to fuels. The insets of (b,c) are the optical image of PAzoMA microspheres and Pt-PAzoMA micromotors, respectively. (e) Self-propulsion mechanism of Pt-PAzoMA in H_2O_2 fuels.

be directly calculated or extracted from experimental MSDs/trajectories.

2.8. Numerical Analysis. The oxygen (O_2) molecular diffusion around the Pt-PAzoMA micromotor is simulated by finite element modeling using COMSOL Multiphysics software (version 5.5). 2D model, transport of diluted species interface, and time-dependent study are chosen here. The catalytic surface is set as the O_2 inflow boundary with 750 mol m^{-3} as a concentration value. The original O_2 value is 0 and the diffusion coefficient was predetermined as 2.42×10^{-9} m^2 s^{-1}. A free triangular mesh with a regular size of unit is used. The O_2 concentration nephograms are simulated at a time step of 1×10^{-4} s and a running time over $0-1 \times 10^{-3}$ s.

3. RESULTS AND DISCUSSION

3.1. Fabrication. The fabrication process of Pt-PAzoMA Janus micromotors with a spherical shape is shown in Figure 1a–d, which includes three steps: the formation of microsphere arrays on cleaned glass slides *via* the reverse breath figure (RBF) method, capping microspheres with a Pt layer on half side through electron beam evaporation (EBE), and releasing microspheres from the substrate by ultrasonification. The RBF method is chosen here for its low-cost, time-saving, easy implementation, and effectivity to fabricate highly ordered microsphere arrays (inset of Figure 1b).[35] The microspheres after EBE are presented in the inset of Figure 1c. After releasing, as illustrated in Figure 1e, Pt-PAzoMA micromotors are transferred into fuels and ready to work, with the help of Pt capping as a catalyst to decompose H_2O_2 and induce the O_2 concentration gradient.[36] The catalytic reaction could be expressed as[37]

$$2H_2O_2 \rightarrow O_2 + 2H_2O \quad (1)$$

3.2. Photodeformation of Pt-PAzoMA Micromotors. Before discussing the motility of Pt-PAzoMA micromotors, their deformability is investigated as it is considered as the basics of motion modulation. With the chemical structures shown in Figure 2a, it is widely recognized that the photoactive azobenzene group goes through *E*/*Z* photo-isomerization, switching from stable *trans* form (straight *E*-isomer) to unstable *cis* form (bent *Z*-isomer) using UV light or blue light within the absorbance range of azobenzene chromophores.[38] On the contrary, when azobenzene groups are irradiated by visible light or heated by temperature above its glass-transition temperature T_g, that is, $T_g \approx 68$ °C (Figure S1) in this work, most of the *cis* azobenzene would be transformed into *trans* form again. The isomerization of the side-chain azobenzene groups in the PAzoMA homopolymer was confirmed by ^{1}H NMR with an obvious peak drift from 7.8 ppm before LPL irradiation to 6.8 ppm after LPL irradiation (Figure S2). The morphology of the spherical Pt-PAzoMA micromotor is presented in Figure 2b, showing the main elemental compositions N, O of the PAzoMA homopolymer, and the half-coating Pt element. After LPL irradiation, as shown in Figure 2c, the micromotors elongate along the LPL direction, with the same elemental distribution before deformation. More SEM and energy-dispersive spectrometry (EDS) characterizations of the elliptical PAzoMA microsphere are shown in Figure S3. By tuning the illumination of LPL or the irradiation time, the aspect ratio of the micromotors could be modulated precisely.[30] Here, we exemplarily choose deformed micromotors after 20 min of LPL irradiation [illumination (613 ± 3) mW cm^{-2}] for the following statistical analysis. The aspect ratio (length of the long axis/length of the short axis) distribution of the deformed Pt-PAzoMA micromotors is shown in Figure 2d, with an average aspect ratio of 1.37. The projected area (the maximum cross area) before and after deformation are presented in Figure 2e. Dividing the average projected area of elliptical micromotors by that of spherical micromotors, a projected area ratio of 1.36 is obtained. The

https://doi.org/10.1021/acsami.1c07569
ACS Appl. Mater. Interfaces 2021, 13, 30106−30117

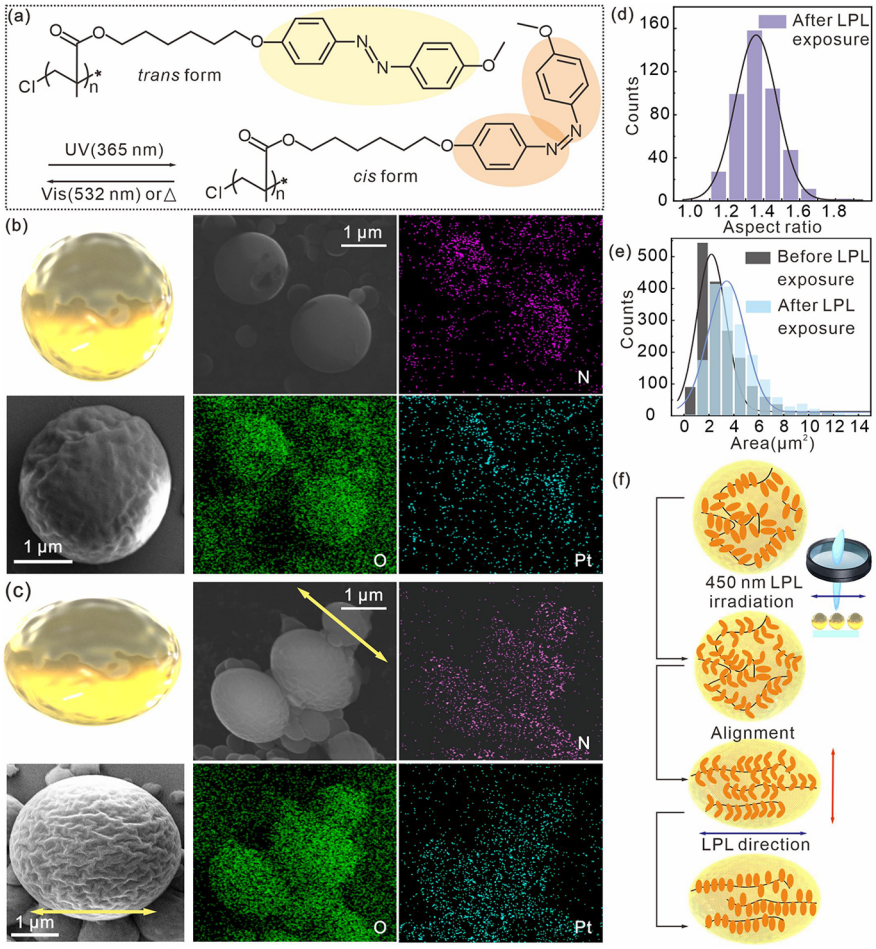

Figure 2. Characterization of Pt-PAzoMA micromotor deformability with an irradiation of 450 nm LPL [illumination (613 ± 3) mW cm^{-2}]. (a) Chemical structures of the PAzoMA homopolymer before and after LPL irradiation showing the photo-isomerization of side-chain azobenzene groups at the PAzoMA homopolymer. (b,c) Scheme and SEM images of micromotors with the corresponding EDS mapping of N, O, and Pt elements (b) before LPL irradiation and (c) after LPL irradiation. The yellow arrow indicates the polarization direction of LPL. (d) Histogram of the aspect ratio (major axis/minor axis) of the deformed Pt-PAzoMA micromotor after LPL irradiation. The solid black curve is the corresponding Gaussian fitting. (e) Projected area distribution of Pt-PAzoMA micromotors before and after LPL irradiation. The two solid curves are corresponding Gaussian fittings. (f) Scheme illustrating the deformation mechanism of the micromotors.

average diameter of micromotors before LPL irradiation is 1.90 μm, which is very close to the diameter of the short axis of the deformed micromotors, that is, 1.89 μm (Figure S4). The statistical data shows that the deformation is nearly unidirectional at the direction of incident LPL, as we expected.

The scheme in Figure 2f is the proposed photo-deformation mechanism of the Pt-PAzoMA micromotors in this work. We propose that the photo-deformation has two steps. The first step is the deformation at the molecular scale where azobenzene groups go through photo-isomerization. It is known that the azobenzene groups are randomly oriented without excitation of LPL.[39] When LPL is applied on the Pt-PAzoMA micromotors, the main axis (*i.e.*, the molecular electric dipole moment) of side-chain azobenzene groups reorients into the direction that is perpendicular to the direction of LPL, which is known as Weigert's effect.[40−42] The probability of azobenzene transformed from *trans* form to *cis* form can also be expressed as follows

$$P = n \cos^2 \theta \tag{2}$$

where θ is the angle between the photoelectric field direction of LPL and direction of azobenzene molecular axial and n is the proportional coefficient. It can be inferred that only when the direction of molecular axial is in the perpendicular direction of LPL, the molecular axial would stop reversible photo-isomerization and finally be stable at this direction. The second step is the photo-deformation at the micromotor scale. Here, to prove that the photo-deformation of micromotor has two steps, it is essential to figure out the differences and relationship between the first step and the second step. Although there are a few theoretical models such as photoinduced molecular diffusion model depicting photo-induced molecular motion in azo polymers, the mechanism of photo-deformation in side-chain azobenzene homopolymer microsphere is still under discussion.[43] Saphiannikova *et al.* provided a photo-deformation theory of LPL-induced high local mechanical stress,[44] which has been experimentally proved by Santer *et al.*[45] and Ryabchun and Bobrovsky *et al.*[38] The theory demonstrated that the backbone of the azo polymer has a strong coupling effect with side-chain azobenzene groups. The photo-alignment of side-chain azobenzene groups, as the driving part, leads to the reorientation of the polymer backbone, causing a locally high stress and finally the elongation of the microsphere along the

https://doi.org/10.1021/acsami.1c07569
ACS Appl. Mater. Interfaces 2021, 13, 30106−30117

LPL direction. This deformation mechanism may also well demonstrate the deformation Pt-PAzoMA micromotors in this work due to the same kind of material and the alike unidirectional deformation along the LPL direction.

To distinguish the two steps in the deformation mechanism, we further use UV−vis characterization to investigate the first photo-isomerization step. The absorbance spectra characterization of PAzoMA homopolymer are presented in Figure 3a.

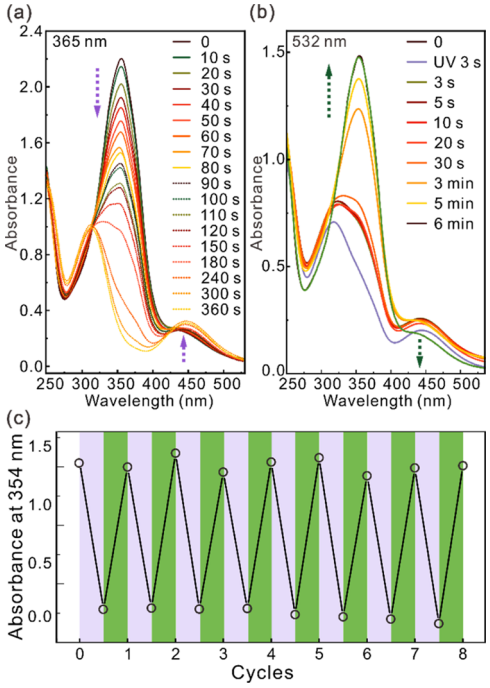

Figure 3. UV−vis characterization of the PAzoMA homopolymer. (a) UV−vis curves representing the *trans* to *cis* transformation of PAzoMA under 365 nm UV light [illumination (0.1 ± 0.05) mW cm^{-1}]. (b) UV−vis curves showing the *cis* to *trans* transformation of the PAzoMA homopolymer under a 532 nm green laser [illumination (19.7 ± 0.1) mW cm^{-1}]. The UV irradiation illumination is (27.9 ± 0.1) mW cm^{-1}. (c) Absorption changes under alternating 365 nm UV irradiation [3 s, illumination (27.9 ± 0.1) mW cm^{-1}] and 532 nm visible light [6 min, illumination (19.7 ± 0.1) mW cm^{-1}]. UV irradiation duration and green laser irradiation duration are indicated by purple and green backgrounds, respectively.

With the increase of UV irradiation time, the absorbance at 354 and 446 nm dropped from their peaks, showing a decrease of *trans* form in PAzoMA. The $\pi-\pi^*$ electronic transition corresponds to the peak at 354 nm, while another peak at 446 nm associates with the $n-\pi^*$ electronic transition. The results show that the photo-isomerization cycle could be triggered by 365 nm UV light and 532 nm green light. Without light, the relaxation time from *cis* PAzoMA to *trans* PAzoMA takes 48 h (Figure S5). It is obvious that at a higher light intensity (Figure 3b), the photo-isomerization is a fast process within 3 s. While the photo-deformation of Pt-PAzoMA micromotors takes a few minutes, which indicates that these two processes happen in different time scales. Other literature also notices this phenomenon in azo polymers using UV light at the same wavelength and intensity.[38] It could be explained that although photo-alignment of side-chain azobenzene develops very fast, the mass transportation of the backbone polymer along the direction of LPL is a slower procedure. In other words, to trigger the photo-deformation of Pt-PAzoMA micromotors, enough time of LPL irradiation should be assured to motivate the backbone polymers. As shown in Figure 3c, the switch between UV light and green laser induces the multi-cycles of photo-isomerization, representing a good repetition for potential micromotor deformation.

3.3. Motion Behavior Analysis. We choose deformed micromotors with an aspect ratio of 1.37 for the following trajectory analysis and MSD analysis. The trajectories are the most direct method to investigate the motion of micromotors before and after LPL irradiation. As shown in Figure 4a,b, we present one 60 s trajectory both before and after LPL irradiation on the optical image sequences. From an estimation, the trajectory before motion modulation is slightly longer than the trajectory after motion modulation. In order to eliminate the random error and have a more qualitative insight into the dynamics of Pt-PAzoMA micromotors, we recorded motion trajectories of 20 micromotors over a time scale of 60 s at different concentrations of fuels (Figure S6). All trajectories are color-coded to indicate the time progression of micromotors. The trajectories of undeformed spherical micromotors are longer than that of deformed elliptical micromotors, especially at 12 and 15 wt % concentrations, showing motion differences between the two geometries of robots. At different fuel concentrations, we also show one trajectory both before and after motion regulation in Videos S1−S6.

It is important to figure out the propulsion mechanism for further motion analysis of the catalytic Pt-PAzoMA micromotor. For a non-bimetal or non (metal−TiO_2)-catalytic Janus system as our micromotor in this work, bubble propulsion or self-diffusiophoresis is the most common propulsion mechanism.[46] It is observed that, even in 15 wt % high concentration

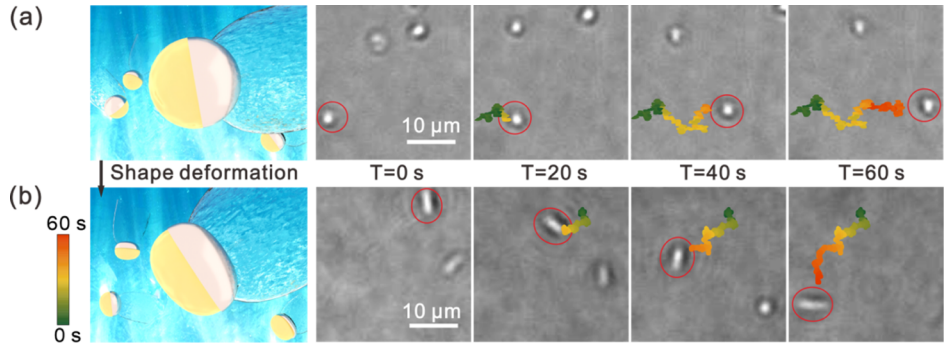

Figure 4. Trajectory tracking of Pt-PAzoMA micromotors. Schematics and corresponding optical image sequences representing the real-time trajectory tracking of Janus micromotors (a) before and (b) after LPL irradiation. The targeted micromotors are indicated by a red circle.

https://doi.org/10.1021/acsami.1c07569
ACS Appl. Mater. Interfaces 2021, 13, 30106−30117

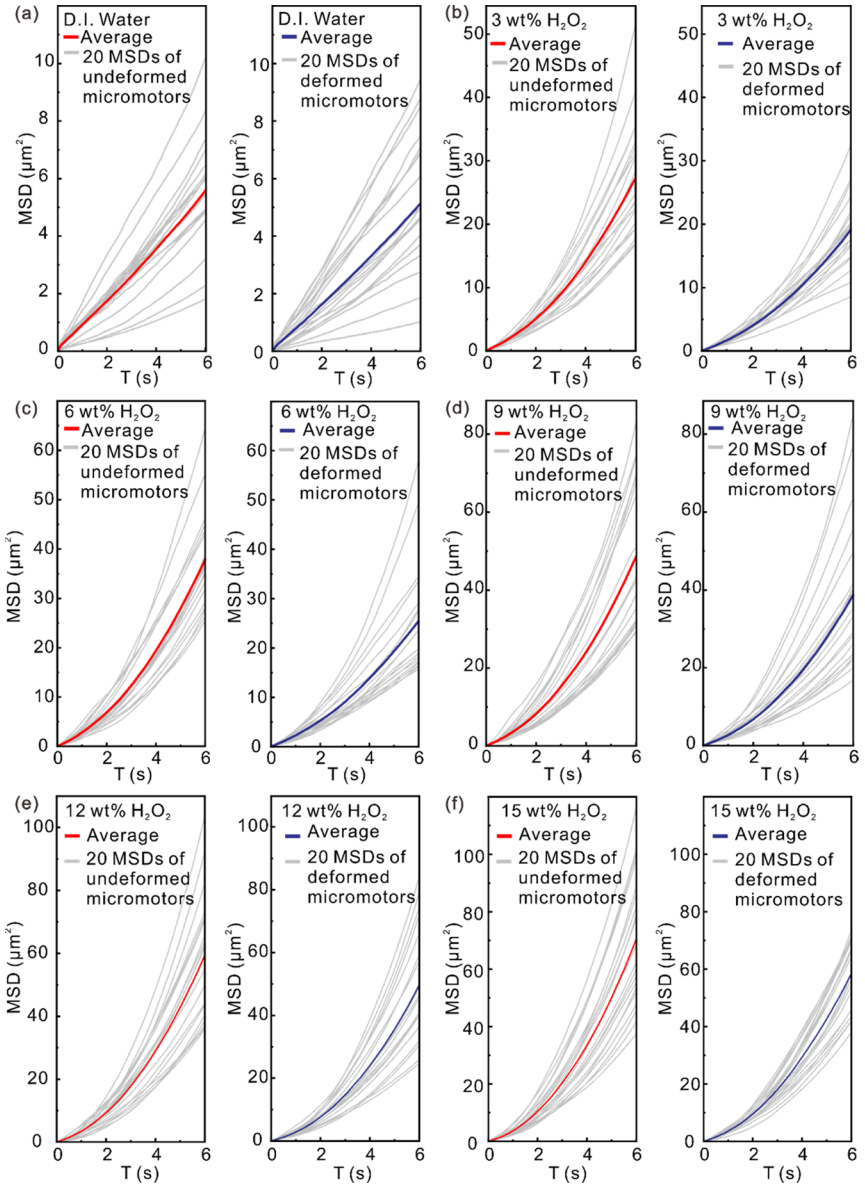

Figure 5. Average MSDs of Pt-PAzoMA micromotors both before (indicated in red) and after LPL irradiation (indicated in blue) under different H_2O_2 concentrations: (a) DI water; (b) 3 wt % H_2O_2; (c) 6 wt % H_2O_2; (d) 9 wt % H_2O_2; (e) 12 wt % H_2O_2; and (f) 15 wt % H_2O_2. Each average MSD (indicated in red or blue) is the average of 20 MSDs (indicated in gray) at the same condition.

of fuels, no oxygen bubble is generated in experiments. This could be due to the small size of the micromotor, with a diameter around 2 μm, which is difficult for the spherical micromachine to nucleate oxygen molecules.[47] In addition, the O_2 concentration gradient during the reaction generating a diffusiophoretic force leads to the propulsion of micromotors.[48] The O_2 concentration gradient is proved by the simulation results using finite element modeling.[49,50] As shown in Figure S7, we can observe that at the Pt side, a strong oxygen gradient is presented, confirming that the propulsion mechanism is self-diffusiophoresis.

We then take standardized procedures of quantitatively evaluating the motion of micromotors by analyzing MSDs. In general, when the tracking video has a total time length L, MSD data is to be considered steps up to $L/10$. The MSD at higher Δt may not be fully trusted for its low statistical power.[20] The data of MSDs here is only presented up to 6 s based on the trajectories (Figure S6) obtained from 60 s tracking movies, which already provides enough data points for calculating the MSD of each micromotors. At each fuel concentration, the MSDs for 20 micromotors before or after LPL irradiation are shown in Figure 5, indicated with gray lines. The average MSDs, indicated by red (before deformation) or blue (after deformation), are taken over all 20 micromotors. The MSD in a 2D projection is given as the most well-known formula[51]

$$\mathrm{MSD} = 4D_T\Delta t + \frac{V^2\tau_R^2}{2}\left[\frac{2\Delta t}{\tau_R} + e^{-2\Delta t/\tau_R} - 1\right] \quad (3)$$

where D_T is the translational diffusion coefficient, τ_R is the time scale of the rotation diffusion coefficient D_R, and V is the propulsive speed. For spherical micromotors and elliptical micromotors, D_T, D_R, τ_R, and V have different expressions. We use subscript characters "s" and "e" here to represent corresponding parameters of spherical and elliptical micro-

https://doi.org/10.1021/acsami.1c07569
ACS Appl. Mater. Interfaces 2021, 13, 30106−30117

motor, respectively. For a spherical micromotor, $D_{Ts} = \frac{k_B T}{6\pi\eta R}$ is the particle translational diffusion coefficient, $D_{Rs} = \tau_{Rs}^{-1} = \frac{k_B T}{8\pi\eta R^3}$ is the rotational diffusion coefficient of the spherical micromotor, V_s is the propulsive speed, and τ_{Rs} is the time scale of rotational diffusion. In the equation of D_{Ts} and D_{Rs}, $k_B T$ is the thermal energy, where k_B is the Boltzmann constant and T is the temperature. R is the radius of the spherical micromotor and η is the viscosity of DI water. For our elliptical micromotors with length $2a$ as the long axis and length $2b$ as the short axis, we have translational diffusion coefficient along the long-axis direction $D_{Tea} = \frac{k_B T}{6\pi\eta a G_a}$, translational diffusion coefficient along the short-axis $D_{Teb} = \frac{k_B T}{6\pi\eta b G_b}$, total translational diffusion coefficient $D_{Te} = \frac{2}{\frac{1}{D_{Tea}} + \frac{1}{D_{Teb}}}$, and rotational diffusion coefficient $D_{Re} = \frac{k_B T}{6\eta\gamma G_\theta}$, where γ is the volume of micromotors, and G_a, G_b, and G_θ are the geometric factors derived from Perrin's equations with aspect ratio φ as the only variable.[52] We can get fitting translational diffusion coefficient D_{Ts}, D_{Te}, and rotational diffusion coefficients τ_{Rs}, τ_{Re} from experimental average MSDs. In DI water (Figure 5a), eq 3 is rewritten as MSD = $4D_T\Delta t$. Using this equation, we could obtain experimental results of translational diffusion coefficients D_{Ts} = 0.227 $\mu m^2/s$ and D_{Te} = 0.211 $\mu m^2/s$. Aspect ratio φ = 1.37, diameter R = 0.949 μm, and the volume of the deformed micromotor V_e = 4.826 μm^3 are adopted from the experiment. Theoretical results of D_{Ts} = 0.231 $\mu m^2/s$ and D_{Te} = 0.178 $\mu m^2/s$ are obtained. The theoretical value of translational diffusion coefficients D_{Ts} and D_{Te} is quantitatively agreeable with the corresponding experiment value, which means the trajectory tracking and MSD results are trustworthy.

As depicted in Figure 6a, we plot the average MSD values under different H_2O_2 concentrations at 6 s. Note that at the same concentration (3, 6, 9, 12, and 15 wt %), the average MSD value of a spherical micromotor (indicated in red) is always larger than that of an elliptical micromotor (indicated in blue), which means there is a factor affecting the motion intensity of micromotors except concentrations. Since the main difference of the micromotors before and after LPL irradiation is the geometries, we attribute the motion change to the micromotor deformation. The following analysis targets on uncovering the effect of different micromotors' geometries (*i.e.*, spherical shape and elliptical shape with an aspect ratio of 1.37) on the motion behavior.

According to eq 3, the differences of MSD mainly come from the differences in speed V due to the small variation of diffusion coefficients between spherical and elliptical micromotors. Speed is also investigated to see the motion differences. A direct average speed comparison is shown in Figure S8, where the average speed of elliptical Janus micromotor V_e is smaller than that of the spherical Janus micromotor V_s at each fuel concentration. To get a more reliable and quantitative analysis of the average speed, the instantaneous speeds from particle trajectories are calculated and averaged using over 2000 frames at each concentration (Figure 6b). We find that the average values of V_s/V_e at each concentration are a constant. By averaging V_s/V_e at all H_2O_2 concentrations, we get the experimental speed ratio V_s/V_e = 1.197 (Figure 7a). An alternative way to get the experimental

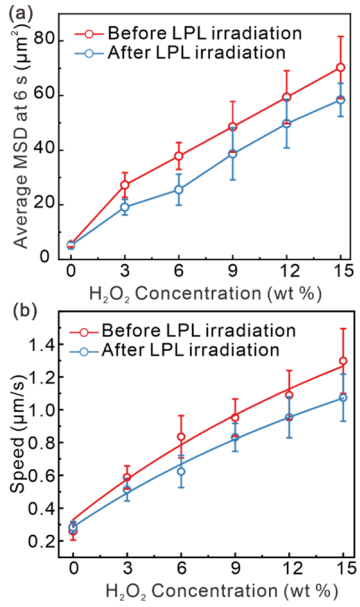

Figure 6. Motion analysis of Pt-PAzoMA micromotors. (a) Value of average MSDs at 6 s before and after LPL irradiation under different H_2O_2 fuel concentrations. (b) Average speed of Pt-PAzoMA micromotors before and after LPL irradiation under different H_2O_2 fuel concentrations. The solid red and blue curves in (b) are the best fitting using eqs 4 and 5.

speed ratio V_s/V_e is to fit the average speed points in Figure 6b by the following equations[51]

$$V = \frac{3\pi}{2} k g \lambda^2 \tag{4}$$

$$k = k_2 \frac{c(H_2O_2)}{c(H_2O_2) + \frac{k_2}{k_1}} \tag{5}$$

Here, g is the hydrodynamic radius defined by the Stokes–Einstein relation. λ is the interaction range between the solute and the micromotor. k is the effective surface reaction rate in the reaction as illustrated by eq 1. k_1, k_2 refer to the per unit area reaction rate during two different stages of the catalytic reaction.[51] $c(H_2O_2)$ has the unit of volume percentage. Combining equations of V and k together, we get a new equation between propulsive speed and fuel concentration for fitting. Two fitting curves of V_s (red fitting line in Figure 6b) and V_e (blue fitting line in Figure 6b) are obtained, and we could get the experimental speed ratio V_s/V_e = 1.188 through dividing the fitting expression of V_s by the fitting expression of V_e.

Next, the theoretical ratio of speed is calculated. According to the Stokes theorem, the drag force of the spherical micromotor $F_{s,drag}$ and the drag force of the elliptical micromotor $F_{e,drag}$ obey the following rules[53]

$$F_{s,drag} = 6\pi\eta r V_s \tag{6}$$

$$F_{e,drag} = 6\pi\eta a V_e G_a \tag{7}$$

Generally speaking, a micromotor is considered to load two kinds of forces, propulsive force and drag force. The drag force consists of inertial force and viscous force. At a low Reynold regime, the inertial force is much smaller than the viscous force

https://doi.org/10.1021/acsami.1c07569
ACS Appl. Mater. Interfaces 2021, 13, 30106−30117

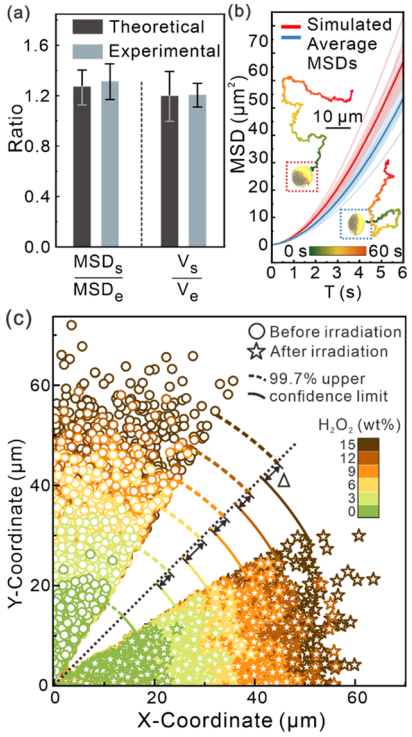

Figure 7. Theoretical values and simulations of trajectories and MSDs of Pt-PAzoMA Janus micromotors. (a) Ratio of average MSD value at 6 s of spherical Janus micromotors (MSD_s) over that of elliptical micromotors (MSD_e); ratio of average speed of spherical micromotors (V_s) over that of elliptical micromotors (V_e). (b) Representative individual (light red/light blue) and corresponding average (red/blue) simulated MSD curves of 20 single Janus micromotors. Red lines represent MSDs of spherical micromotors and blue lines represent MSDs of elliptical micromotors. (c) Last points of simulated trajectories at different fuel concentrations, indicating the differences of motion before and after regulation. The solid/dotted arcs indicate 99.7% upper confidence limit of Gaussian distribution about the distances between simulated last points of spherical/elliptical micromotors' trajectories and origin. Δ is the difference of the 99.7% upper confidence limits before and after deformation under the same fuel concentration.

so that it could be neglected. Assuming that the micromotor achieves stable motion with the net force equals to zero[54]

$$F_{\text{propulsion}} = F_{\text{drag}} \tag{8}$$

For propulsive force at the same fuel concentrations, the O_2 production is linear to the catalytic surface area.[55] The propulsive force worked on the micromotor is proportional to the concentration gradient of O_2 molecules

$$F_{\text{propulsion}} = mS_{\text{Pt}} \tag{9}$$

where m is the constant and S_{Pt} is the Pt-evaporated area. The Pt-evaporated area of the spherical micromotor $S_{\text{s,Pt}}$ and elliptical micromotor $S_{\text{e,Pt}}$ is expressed as follows

$$S_{\text{s,Pt}} = 2\pi r^2 \tag{10}$$

$$S_{\text{e,Pt}} = \frac{2}{3}\pi(2ab + b^2) \tag{11}$$

According to eqs 6−11, we have

$$\frac{V_s}{V_e} = \frac{3\varphi G_a S_{\text{s,Pt}}}{S_{\text{e,Pt}}\left(2 + \frac{1}{\varphi}\right)} \tag{12}$$

Taken experimentally extracted parameters φ = 1.37, $S_{\text{s,Pt}}/S_{\text{e,Pt}}$ = 0.738, G_a = 1.075 into eq 12, we could obtain the theoretical results of V_s/V_e = 1.20, which is very close to the experimental result of 1.197 (by simply averaging the speed) or 1.188 (by fitting), as shown in Figure 7a. From eq 12, we find that the motion intensity is affected by aspect ratio φ and geometry factor G_a, which would change with the deformation under LPL motion control signal input.

We put the theoretical and experimental value of MSD ratio MSD_s/MSD_e and speed ratio V_s/V_e in Figure 7a to get a more direct view. Within the limit of errors, the experimental data is consistent with the theoretical data. The MSD ratio and speed ratio show that the motion of the Pt-PAzoMA micromotors after LPL irradiation slows down.

In addition, average MSDs and trajectories are simulated and compared with the experimental results. A similar motion intensity change before and after motion regulation is captured by the molecular dynamics simulation of MSDs and trajectories. For a spherical Janus micromotor with radius R = 0.949 μm at room temperature, experimental results D_{Ts} = 0.231 $\mu m^2/s$, D_{Rs} = 0.192 rad^2/s were used in the trajectory simulation. For an elliptical Janus micromotor with long-axis $2a$ = 1.29 μm, experimental results D_{Te} = 0.211 $\mu m^2/s$ and D_{Re} = 0.127 rad^2/s were used in the molecular dynamics simulation. As shown in Figure 7b, the simulated MSDs before and after LPL irradiation in 15 wt % fuel concentration show the same regulation with the experiment results (Figure 5f), where the red MSD curve is above the blue MSD curve within the observation time. The differences in MSDs could be visually reflected in the corresponding trajectories inside Figure 7b. The deformed micromotor (indicated by the blue dotted rectangular) after regulation shows a slower motion with a shorter trajectory than the undeformed micromotor (indicated by the red dotted rectangular) before regulation. We further extract the final points of simulated 60 s trajectories both before and after motion regulation under different fuel concentrations, where the trajectories are assumed to start at the same origin (0,0). At each concentration both before and after motion regulation, 1×10^5 last points of the simulated trajectories were extracted and around 10^4 last points are shown in Figure 7c. We only show points within an arc of 30° which is enough to show the motion differences due to the isotropic motion. The upper limit of 3σ confidence intervals of Gaussian distribution about distances between simulated points and original points is shown by the arc (center at the origin) with various colors indicating different fuel concentrations. At each H_2O_2 concentration, the distance between the 99.7% points and the origin is indicated by the radius range of the corresponding arc. The radium of the arc directly reflects the motion intensity. At the same fuel concentration, after blue light signal illuminating, our micromotor shows a weaker motion with a smaller arc radius. The figure presents a precise motion regulation of Pt-PAzoMA micromotors that happens with shorter trajectories after the LPL irradiation.

3.4. Discussion. Most works are dedicated to improve the efficiency of micromotors by increasing the micromotors' speeds. The speed-up can fasten micromotors to the targeted places, while the speed-down enables micromotors to linger around the targeted place for long-term operation. The

https://doi.org/10.1021/acsami.1c07569
ACS Appl. Mater. Interfaces 2021, 13, 30106−30117

slowdown in motion also benefits micromotors in diverse applications.

Through the motion analysis of Pt-PAzoMA micromotors, it could be concluded that the motion of micromotors is modulated by the drag force through geometry alteration. Given a proper signal (450 nm LPL), the photo-alignment of side-chain azobenzene groups can induce photo-deformation of Pt-PAzoMA micromotors and keep that shape until receiving the next deformation signal. Seeing the versatility of the drag force controlling behavior in Pt-PAzoMA micromotors, we put forward a motion control concept. According to the concept, motion is able to be changed precisely through deformation under one brief external signal and the following motion modulation need no continuous signal input. This motion regulation is a "switch" type modulation that alters the drag force by the input signal acting as switch. The stability and energy-saving capability of this strategy are very attractive for micromotors to be used in signal/power limited places for a long term.

We further discuss about the potential advantages, preconditions, and application scenarios for motion control through drag force manipulation. The first potential advantage is the stability of keeping the altered motion state. Most deformable micromotors could not preserve desired shapes without continuous motion control signals.[56] Such micromotors' shapes are volatile especially under a disconnection with control signals, as shown in the left side of Scheme 1

Scheme 1. Schematic Illustration Showing Two Different Motion Control Routes by Altering Propulsive Force (Indicated in Blue) and by Altering Drag Force (Indicated in Green)

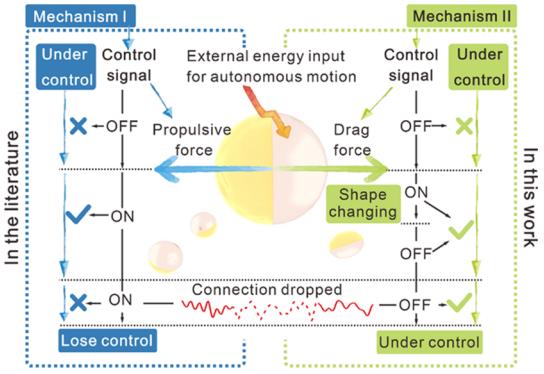

(Mechanism I). On the other hand, some micromotors are capable of maintaining the deformation induced by a brief deformation signal, like the Pt-PAzoMA micromotor in this work. This characteristic provides Pt-PAzoMA micromotors with stability in motion regulation without the participation of continuous control signals (Mechanism II, Scheme 1).

The other potential advantage is the energy-saving capability. This advantage comes from the motion control needing no continuous signal and thus the signal controlling power can be saved. For flying squirrel, gliding by changing its shape is an energy-efficient way to reach a far destination. For aircraft, changing the wings shape to alter its air drag could make the fuel consumption to the minimum extent. For micromotors assigned with long-time operations, this motion regulation method has potential to help the micromachine to save energy and perform long-term tasks. In another word, minimum motion controlling power consumption could be achieved.

Although using drag force as the motion switch has many potential advantages, prerequisites do exist. There are two preconditions to apply this motion control method: (1) the micromotor can maintain the deformed shape for a desired long time after the signal-inducing deformation occurs. Without shape retainability, the drag force cannot be precisely tuned and stay at a desired level with minimum signal reception. Not only PAzoMA can meet the precondition, a wide range of functional materials such as shape memory alloy and shape memory polymer could also satisfy this criterion for their capability to deform into a temporary stable shape.[57] (2) Control signal power is independent with the external power for propulsion. The motion control signals could be either independent[58] or dependent[28] from the external stimuli for self-propulsion. If the micromotor has propulsive signal that is unrelated with control signal, there are two possible results. For micromotors with no shape retainability, the drop of control signal would disturb its movement, while for those shape-retainable micromotors, the movement adjustment could be maintained. When the motion control signal is inseparable with the propulsive stimuli, the disconnection with the motion control signal also means a stop of self-propulsion, whether having shape retainability or not. Only in the design that control power is separated with power for self-propulsion, the drag force-controlled regulation can show its advantages, as illustrated in Scheme 1. In this work, importantly, Pt-PAzoMA micromotors could maintain the shape after the motion control signal. What is more, the motion control system, that is, light field, is separated from its propulsion system, that is, chemical gradient field.

Satisfying the two preconditions, how could we take advantages of drag force manipulation strategy and apply it into specific application scenarios? From one perspective, the stability of the strategy allows discontinuous control signal/a minimum control signal input. The stable motion control method proposed in this work is a robust alternative for micromotors working in a large water field that could easily run out of signal receiving region or for micromotors used *in vivo* with a signal screening environment that are difficult for certain signals to perfectly reach. For instance, magnetic or acoustic controlled nano-/micromotors have been widely tested in lab rats, either for drug delivery or for tumor cell destruction.[59,60] However, for real *in vivo* application, long-time navigation through continuous magnetic/acoustic signals may limit the movements of patients within the working range of medical equipment or bring side effects to patients. The drag force-manipulated motion control can alleviate these problems by switching to the desired mode and stay at the mode without further continuously signal input, which means the patients have freedom of movements and less risks of side effects by using brief signals to control the micromotorics instead of continuous input. From another perspective, minimum power consumption can be achieved due to the minimum control input, which provides our motion control strategy with diverse opportunities for applications need energy-saving, mostly long-term operation robotics or swarm robotics. One interesting application scenario is, when we want to release drug locally around a targeted organ, it is important to leave the micromotor around the target. The micromotor kept in fast speed is hard to continuously release drug molecules to get nearby cells for the difficulty in the confinement of moving

https://doi.org/10.1021/acsami.1c07569
ACS Appl. Mater. Interfaces 2021, 13, 30106−30117

areas. By controllably slowing down the speed of micromotors, we can optimize the drug diffusion efficiency of our micromotors for long-term efficient drug release. Besides, for long-time diseased area monitoring, slowing micromotor down is a strategy to localize the motion of the micromotors. In the desired long time, most of the micromotors can only travel inside the targeted area, wander slowly, and perform their tasks.

4. CONCLUSIONS

In summary, Pt-PAzoMA light-deformable Janus micromotors are fabricated by the low-cost RBF methods together with the EBE process. Using the spherical micromotor as a representative, we show that the LPL (450 nm) induces stable photo-deformation of the micromotor from a spherical shape to an elliptical shape. Inspired by flying squirrel in its landing movement, motion change of the deformed Pt-PAzoMA Janus micromotor is observed and revealed by the trajectory tracking and the MSD curves of the micromotors. The elliptical micromotor is slowed down with shorter trajectories and smaller MSD values, which is further proved by the simulations of trajectories and MSDs. Using the experimental results and theoretical calculation, the movements are proved to be changed by the increased drag force which is affected through varied geometries. Namely, motion of the Pt-PAzoMA micromotor could be altered by manipulating the drag force through precise geometry change.

Based on the Pt-PAzoMA micromotors' experiments, a different motion control strategy is proposed for micromotors (see Discussion section). The strategy is to manipulate the motion of the micromotor through switching drag force by deformation that could be maintained for a long term without a continuous signal input. To apply this regulation method, micromotors are required to have a stable shape retaining capability after deformation. The advantage for the method is that a continuous control signal could be avoided and the regulation is stable for a long term, minimizing the energy input for regulation. This work paves the way to construct an alteration of motion control method through drag force manipulation with stability, which has superior potential to be adopted in application scenarios like working in areas where the signal input is limited, long-term operation with an energy-saving need. Future research directions include combining the motion control method with minimum power consumption, faster responses, and stability for application scenarios such as long-time drug delivery, detection, and microsurgery.

■ ASSOCIATED CONTENT

Supporting Information

The Supporting Information is available free of charge at https://pubs.acs.org/doi/10.1021/acsami.1c07569.

Motion recording of undeformed and deformed Pt-PAzoMA micromotors in DI water (AVI)

Motion recording of undeformed and deformed Pt-PAzoMA micromotors in 3 wt % H_2O_2 (AVI)

Motion recording of undeformed and deformed Pt-PAzoMA micromotors in 6 wt % H_2O_2 (AVI)

Motion recording of undeformed and deformed Pt-PAzoMA micromotors in 9 wt % H_2O_2 (AVI)

Motion recording of undeformed and deformed Pt-PAzoMA micromotors in 12 wt % H_2O_2 (AVI)

Motion recording of undeformed and deformed Pt-PAzoMA micromotors in 15 wt % H_2O_2 (AVI)

DSC spectrum of *trans* and *cis* form PAzoMA microspheres (Figure S1); ^{1}H NMR of *trans* and *cis* form PAzoMA solution proving the photo-transformation process (Figure S2); SEM and EDS characterization of the deformed PAzoMA microsphere (Figure S3); histograms showing diameter distributions of undeformed and deformed Pt-PAzoMA micromotors (Figure S4); UV−vis characterization of the PAzoMA homopolymer showing the relaxation of *cis* form side-chain azobenzene groups in the dark environment (Figure S5); 10 trajectories of the Janus micromotors both before and after motion alteration under each fuel concentration (Figure S6); Simulation of O_2 concentration distribution produced by Pt-PAzoMA micromotor (Figure S7); and comparison of average speeds of deformed and undeformed Janus micromotors at different fuel concentrations (Figure S8) (PDF)

■ AUTHOR INFORMATION

Corresponding Authors

Shaoliang Lin − *Shanghai Key Laboratory of Advanced Polymeric Materials, Key Laboratory for Ultrafine Materials of Ministry of Education, School of Materials Science and Engineering, East China University of Science and Technology, Shanghai 200237, China;* orcid.org/0000-0003-3374-9934; Email: slin@ecust.edu.cn

Yongfeng Mei − *Department of Materials Science, Fudan University, Shanghai 200433, P. R. China;* orcid.org/0000-0002-3314-6108; Email: yfm@fudan.edu.cn

Authors

Xinyi Lin − *Department of Materials Science, Fudan University, Shanghai 200433, P. R. China*

Borui Xu − *Department of Materials Science, Fudan University, Shanghai 200433, P. R. China;* orcid.org/0000-0001-5357-0400

Zhe Zhao − *Department of Materials Science, Fudan University, Shanghai 200433, P. R. China*

Xiaoyan Yang − *Shanghai Key Laboratory of Advanced Polymeric Materials, Key Laboratory for Ultrafine Materials of Ministry of Education, School of Materials Science and Engineering, East China University of Science and Technology, Shanghai 200237, China*

Yi Xing − *State Key Laboratory of Molecular Engineering of Polymers, Department of Macromolecular Science, Fudan University, Shanghai 200433, China*

Chunyu You − *Department of Materials Science, Fudan University, Shanghai 200433, P. R. China*

Ye Kong − *Department of Materials Science, Fudan University, Shanghai 200433, P. R. China*

Jizhai Cui − *Department of Materials Science, Fudan University, Shanghai 200433, P. R. China*

Liangliang Zhu − *State Key Laboratory of Molecular Engineering of Polymers, Department of Macromolecular Science, Fudan University, Shanghai 200433, China;* orcid.org/0000-0001-6268-3351

Complete contact information is available at: https://pubs.acs.org/10.1021/acsami.1c07569

Author Contributions

All authors discussed about the data and revised the manuscript. L.X., X.B., C.J., and M.Y. proposed the idea. Y.X. fabricated microsphere samples under the supervision of L.S. X.Y. characterized the sample using DSC and ^{1}H NMR under the supervision of Z.L. L.X. fabricated micromotors and tracked the motion behavior of these micromotors under different conditions. X.B. and L.X. performed simulations. L.X. calculated theoretical values, prepared figures, and wrote the manuscript. Z.Z., Y.C., and K.Y. revised the manuscript.

Notes

The authors declare no competing financial interest.

■ ACKNOWLEDGMENTS

This work was supported by the National Natural Science Foundation of China (51961145108, 61975035, and 52073092), Science and Technology Commission of Shanghai Municipality (17JC1401700), and the Program of Shanghai Academic Research Leader (19XD1400600).

■ REFERENCES

(1) Guix, M.; Mayorga-Martinez, C. C.; Merkoçi, A. Nano/Micromotors in (Bio)chemical Science Applications. *Chem. Rev.* **2014**, *114*, 6285−6322.

(2) Draz, M. S.; Kochehbyoki, K. M.; Vasan, A.; Battalapalli, D.; Sreeram, A.; Kanakasabapathy, M. K.; Kallakuri, S.; Tsibris, A.; Kuritzkes, D. R.; Shafiee, H. DNA Engineered Micromotors Powered by Metal Nanoparticles for Motion Based Cellphone Diagnostics. *Nat. Commun.* **2018**, *9*, 4282.

(3) Zhang, Q.; Dong, R.; Chang, X.; Ren, B.; Tong, Z. Spiropyran-Decorated SiO2-Pt Janus Micromotor: Preparation and Light-Induced Dynamic Self-Assembly and Disassembly. *ACS Appl. Mater. Interfaces* **2015**, *7*, 24585−24591.

(4) Solovev, A. A.; Xi, W.; Gracias, D. H.; Harazim, S. M.; Deneke, C.; Sanchez, S.; Schmidt, O. G. Self-Propelled Nanotools. *ACS Nano* **2012**, *6*, 1751−1756.

(5) Esteban-Fernández de Ávila, B.; Angsantikul, P.; Li, J.; Gao, W.; Zhang, L.; Wang, J. Micromotors Go In Vivo: From Test Tubes to Live Animals. *Adv. Funct. Mater.* **2018**, *28*, 1705640.

(6) Lin, X.; Xu, B.; Zhu, H.; Liu, J.; Solovev, A.; Mei, Y. Requirement and Development of Hydrogel Micromotors towards Biomedical Applications. *Research* **2020**, *2020*, 1−15.

(7) de Ávila, B. E.-F.; Angsantikul, P.; Li, J.; Angel Lopez-Ramirez, M.; Ramírez-Herrera, D. E.; Thamphiwatana, S.; Chen, C.; Delezuk, J.; Samakapiruk, R.; Ramez, V.; Obonyo, M.; Zhang, L.; Wang, J. Micromotor-Enabled Active Drug Delivery for In Vivo Treatment of Stomach Infection. *Nat. Commun.* **2017**, *8*, 272.

(8) Jurado-Sánchez, B.; Pacheco, M.; Rojo, J.; Escarpa, A. Magnetocatalytic Graphene Quantum Dots Janus Micromotors for Bacterial Endotoxin Detection. *Angew. Chem., Int. Ed.* **2017**, *56*, 6957−6961.

(9) Jurado-Sánchez, B.; Wang, J. Micromotors for Environmental Applications: a Review. *Environ. Sci.: Nano* **2018**, *5*, 1530−1544.

(10) Eskandarloo, H.; Kierulf, A.; Abbaspourrad, A. Nano-and Micromotors for Cleaning Polluted Waters: Focused Review on Pollutant Removal Mechanisms. *Nanoscale* **2017**, *9*, 13850−13863.

(11) Lin, X.; Zhu, H.; Zhao, Z.; You, C.; Kong, Y.; Zhao, Y.; Liu, J.; Chen, H.; Shi, X.; Makarov, D.; Mei, Y. Hydrogel-Based Janus Micromotors Capped with Functional Nanoparticles for Environmental Applications. *Adv. Mater. Technol.* **2020**, *5*, 2000279.

(12) Xie, H.; Sun, M.; Fan, X.; Lin, Z.; Chen, W.; Wang, L.; Dong, L.; He, Q. Reconfigurable Magnetic Microrobot Swarm: Multimode Transformation, Locomotion, and Manipulation. *Sci. Robot.* **2019**, *4*, No. eaav8006.

(13) Chowdhury, S.; Jing, W.; Cappelleri, D. J. Controlling Multiple Microrobots: Recent Progress and Future Challenges. *J. Micro-Bio Robot.* **2015**, *10*, 1−11.

(14) Teo, W. Z.; Pumera, M. Motion Control of Micro-/Nanomotors. *Chem.—Eur. J.* **2016**, *22*, 14796−14804.

(15) Liu, L.; Bai, T.; Chi, Q.; Wang, Z.; Xu, S.; Liu, Q.; Wang, Q. How to Make a Fast, Efficient Bubble-Driven Micromotor: A Mechanical View. *Micromachines* **2017**, *8*, 267.

(16) Khalil, I. S. M.; Magdanz, V.; Sanchez, S.; Schmidt, O. G.; Misra, S. Precise Localization and Control of Catalytic Janus Micromotors using Weak Magnetic Fields. *Int. J. Adv. Robot. Syst.* **2015**, *12*, 2.

(17) Mou, F.; Pan, D.; Chen, C.; Gao, Y.; Xu, L.; Guan, J. Magnetically Modulated Pot-Like MnFe2O4 Micromotors: Nanoparticle Assembly Fabrication and their Capability for Direct Oil Removal. *Adv. Funct. Mater.* **2015**, *25*, 6173−6181.

(18) Dong, R.; Zhang, Q.; Gao, W.; Pei, A.; Ren, B. Highly Efficient Light-Driven TiO_2-Au Janus Micromotors. *ACS Nano* **2016**, *10*, 839−844.

(19) Hu, Y.; Liu, W.; Sun, Y. Multiwavelength Phototactic Micromotor with Controllable Swarming Motion for "Chemistry-on-the-Fly". *ACS Appl. Mater. Interfaces* **2020**, *12*, 41495−41505.

(20) Wang, X.; Baraban, L.; Nguyen, A.; Ge, J.; Misko, V. R.; Tempere, J.; Nori, F.; Formanek, P.; Huang, T.; Cuniberti, G.; Fassbender, J.; Makarov, D. High-Motility Visible Light-Driven Ag/AgCl Janus Micromotors. *Small* **2018**, *14*, 1803613.

(21) Jang, B.; Hong, A.; Kang, H. E.; Alcantara, C.; Charreyron, S.; Mushtaq, F.; Pellicer, E.; Büchel, R.; Sort, J.; Lee, S. S.; Nelson, B. J.; Pané, S. Multiwavelength Light-Responsive Au/B-TiO_2 Janus Micromotors. *ACS Nano* **2017**, *11*, 6146−6154.

(22) Maric, T.; Nasir, M. Z. M.; Webster, R. D.; Pumera, M. Tailoring Metal/TiO_2 Interface to Influence Motion of Light-Activated Janus Micromotors. *Adv. Funct. Mater.* **2020**, *30*, 1908614.

(23) Hansen-Bruhn, M.; de Ávila, B. E.; Beltrán-Gastélum, M.; Zhao, J.; Ramírez-Herrera, D. E.; Angsantikul, P.; Gothelf, K. V.; Zhang, L.; Wang, J. Active Intracellular Delivery of a Cas9/sgRNA Complex Using Ultrasound-Propelled Nanomotors. *Angew. Chem., Int. Ed.* **2018**, *57*, 2657−2661.

(24) Shin, S. R.; Migliori, B.; Miccoli, B.; Li, Y. C.; Mostafalu, P.; Seo, J.; Mandla, S.; Enrico, A.; Antona, S.; Sabarish, R.; Zheng, T.; Pirrami, L.; Zhang, K.; Zhang, Y. S.; Wan, K. T.; Demarchi, D.; Dokmeci, M. R.; Khademhosseini, A. Electrically Driven Microengineered Bioinspired Soft Robots. *Adv. Mater.* **2018**, *30*, 1704189.

(25) Tu, Y.; Peng, F.; Sui, X.; Men, Y.; White, P. B.; van Hest, J. C. M.; Wilson, D. A. Self-Propelled Supramolecular Nanomotors with Temperature-Responsive Speed Regulation. *Nat. Chem.* **2017**, *9*, 480−486.

(26) Cheng, Y. C.; Lu, H. C.; Lee, X.; Zeng, H.; Priimagi, A. Kirigami-Based Light-Induced Shape-Morphing and Locomotion. *Adv. Mater.* **2020**, *32*, 1906233.

(27) Ren, Z.; Hu, W.; Dong, X.; Sitti, M. Multi-Functional Soft-Bodied Jellyfish-Like Swimming. *Nat. Commun.* **2019**, *10*, 2703.

(28) Cui, J.; Huang, T.-Y.; Luo, Z.; Testa, P.; Gu, H.; Chen, X.-Z.; Nelson, B. J.; Heyderman, L. J. Nanomagnetic Encoding of Shape-Morphing Micromachines. *Nature* **2019**, *575*, 164−168.

(29) Alapan, Y.; Karacakol, A. C.; Guzelhan, S. N.; Isik, I.; Sitti, M. Reprogrammable Shape Morphing of Magnetic Soft Machines. *Sci. Adv.* **2020**, *6*, No. eabc6414.

(30) Gao, F.; Yao, Y.; Wang, W.; Wang, X.; Li, L.; Zhuang, Q.; Lin, S. Light-Driven Transformation of Bio-Inspired Superhydrophobic Structure via Reconfigurable PAzoMA Microarrays: From Lotus Leaf to Rice Leaf. *Macromolecules* **2018**, *51*, 2742−2749.

(31) Ma, X.; Hortelao, A. C.; Miguel-López, A.; Sánchez, S. Bubble-Free Propulsion of Ultrasmall Tubular Nanojets Powered by Biocatalytic Reactions. *J. Am. Chem. Soc.* **2016**, *138*, 13782−13785.

(32) Jaqaman, K.; Loerke, D.; Mettlen, M.; Kuwata, H.; Grinstein, S.; Schmid, S. L.; Danuser, G. Robust Single-Particle Tracking in Live-Cell Time-Lapse Sequences. *Nat. Methods* **2008**, *5*, 695−702.

(33) Wang, X.; Baraban, L.; Misko, V. R.; Nori, F.; Huang, T.; Cuniberti, G.; Fassbender, J.; Makarov, D. Visible Light Actuated Efficient Exclusion Between Plasmonic Ag/AgCl Micromotors and Passive Beads. *Small* **2018**, *14*, 182537.

https://doi.org/10.1021/acsami.1c07569
ACS Appl. Mater. Interfaces 2021, 13, 30106−30117

(34) Volpe, G.; Gigan, S.; Volpe, G. Simulation of the Active Brownian Motion of a Microswimmer. *Am. J. Physiol.* **2014**, *82*, 659−664.
(35) Zhang, A.; Bai, H.; Li, L. Breath Figure: A Nature-Inspired Preparation Method for Ordered Porous Films. *Chem. Rev.* **2015**, *115*, 9801−9868.
(36) Chen, P. Y.; Keh, H. J. Diffusiophoresis of A Colloidal Sphere in Nonelectrolyte Gradients Parallel to One or TwoPlane Walls. *Chem. Eng. Sci.* **2002**, *57*, 2885−2899.
(37) Serra-Maia, R.; Bellier, M.; Chastka, S.; Tranhuu, K.; Subowo, A.; Rimstidt, J. D.; Usov, P. M.; Morris, A. J.; Michel, F. M. Mechanism and Kinetics of Hydrogen Peroxide Decomposition on Platinum Nanocatalysts. *ACS Appl. Mater. Interfaces* **2018**, *10*, 21224−21234.
(38) Ryabchun, A.; Bobrovsky, A. Photocontrollable Deformations of Polymer Particles in Elastic Matrix. *Adv. Opt. Mater.* **2019**, *7*, 1901486.
(39) Bobrovsky, A.; Ryabchun, A.; Medvedev, A.; Shibaev, V. Ordering Phenomena and Photoorientation Processes in Photochromic Thin Films of LC Chiral Azobenzene-Containing Polymer Systems. *J. Photochem. Photobiol., A* **2009**, *206*, 46−52.
(40) Wang, W.; Du, C.; Wang, X.; He, X.; Lin, J.; Li, L.; Lin, S. Directional Photomanipulation of Breath Figure Arrays. *Angew. Chem., Int. Ed.* **2014**, *53*, 12116−12119.
(41) Li, Y.; He, Y.; Tong, X.; Wang, X. Photoinduced Deformation of Amphiphilic Azo Polymer Colloidal Spheres. *J. Am. Chem. Soc.* **2005**, *127*, 2402−2403.
(42) Li, J.; Chen, L.; Xu, J.; Wang, K.; Wang, X.; He, X.; Dong, H.; Lin, S.; Zhu, J. Photoguided Shape Deformation of Azobenzene-Containing Polymer Microparticles. *Langmuir* **2015**, *31*, 13094−13100.
(43) Juan, M. L.; Plain, J.; Bachelot, R.; Royer, P.; Gray, S. K.; Wiederrecht, G. P. Multiscale Model for Photoinduced Molecular Motion in Azo Polymers. *ACS Nano* **2009**, *3*, 1573−1579.
(44) Petrova, T.; Toshchevikov, V.; Saphiannikova, M. Light-Induced Deformation of Polymer Networks Containing Azobenzene Chromophores and Liquid Crystalline Mesogens. *Soft Matter* **2015**, *11*, 3412−3423.
(45) Di Florio, G.; Bründermann, E.; Yadavalli, N. S.; Santer, S.; Havenith, M. Graphene Multilayer as Nanosized Optical Strain Gauge for Polymer Surface Relief Gratings. *Nano Lett.* **2014**, *14*, 5754−5760.
(46) Zhang, Y. F.; Hess, H. Chemically-Powered Swimming and Diffusion in The Microscopic World. *Nat. Rev. Chem.* **2021**, 1−11, DOI: 10.1038/s41570-021-00281-6.
(47) Zhang, J.; Zheng, X.; Cui, H.; Silber-Li, Z. The Self-Propulsion of the Spherical Pt-SiO_2 Janus Micro-Motor. *Micromachines* **2017**, *8*, 123.
(48) Popescu, M. N.; Uspal, W. E.; Dietrich, S. Self-Diffusiophoresis of Chemically Active Colloids. *Eur. Phys. J.: Spec. Top.* **2016**, *225*, 2189−2206.
(49) Zhang, X.; Xie, W.; Wang, H.; Zhang, Z. Magnetic Matchstick Micromotors with Switchable Motion Modes. *Chem. Commun.* **2021**, *57*, 3797−3800.
(50) Li, J.; Liu, W.; Wang, J.; Rozen, I.; He, S.; Chen, C.; Kim, H. G.; Lee, H. J.; Lee, H. B. R.; Kwon, S. H.; Li, T.; Li, L.; Wang, J.; Mei, Y. Nanoconfined Atomic Layer Deposition of TiO 2 /Pt Nanotubes: Toward Ultrasmall Highly Efficient Catalytic Nanorockets. *Adv. Funct. Mater.* **2017**, *27*, 1700598.
(51) Howse, J. R.; Jones, R. A. L.; Ryan, A. J.; Gough, T.; Vafabakhsh, R.; Golestanian, R. Self-motile colloidal particles: From Directed Propulsion to Random Walk. *Phys. Rev. Lett.* **2007**, *99*, 048102.
(52) Han, Y.; Alsayed, A.; Nobili, M.; Yodh, A. G. Quasi-Two-Dimensional Diffusion of Single Ellipsoids: Aspect Ratio and Confinement Effects. *Phys. Rev. A: At., Mol., Opt. Phys.* **2009**, *80*, 011403.
(53) Shemi, O.; Solomon, M. J. Self-Propulsion and Active Motion of Janus Ellipsoids. *J. Phys. Chem. B* **2018**, *122*, 10247−10255.
(54) Li, L.; Wang, J.; Li, T.; Song, W.; Zhang, G. A Unified Model of Drag Force for Bubble-Propelled Catalytic Micro/nano-motors with Different Geometries in Low Reynolds Number Fows. *J. Appl. Phys.* **2015**, *117*, 104308.
(55) Li, J.; Huang, G.; Ye, M.; Li, M.; Liu, R.; Mei, Y. Dynamics of Catalytic Tubular Mmicrojet Engines: Dependence on Geometry and Chemical Environment. *Nanoscale* **2011**, *3*, 5083−5089.
(56) Tian, Z.; Xu, B.; Wan, G.; Han, X.; Di, Z.; Chen, Z.; Mei, Y. Gaussian-Preserved, Non-Volatile Shape Morphing in Three-Dimensional Microstructures for Dual-Functional Electronic Devices. *Nat. Commun.* **2021**, *12*, 509.
(57) Lendlein, A.; Gould, O. E. C. Reprogrammable Recovery and Actuation Behaviour of Shape-Memory Polymers. *Nat. Rev. Mater.* **2019**, *4*, 116−133.
(58) Su, Y.; Ge, Y.; Liu, L.; Zhang, L.; Liu, M.; Sun, Y.; Zhang, H.; Dong, B. Motion-Based pH Sensing Based on the Cartridge-Case-like Micromotor. *ACS Appl. Mater. Interfaces* **2016**, *8*, 4250−4257.
(59) Li, J.; Li, X.; Luo, T.; Wang, R.; Liu, C.; Chen, S.; Li, D.; Yue, J.; Cheng, S.-h.; Sun, D. Development of A Magnetic Microrobot for Carrying and Delivering Targeted Cells. *Sci. Robot.* **2018**, *3*, No. eaat8829.
(60) Gao, C.; Lin, Z.; Wang, D.; Wu, Z.; Xie, H.; He, Q. Red Blood Cell-Mimicking Micromotor for Active Photodynamic Cancer Therapy. *ACS Appl. Mater. Interfaces* **2019**, *11*, 23392−23400.